

INFERENCE OF HEATING PROPERTIES FROM “HOT” NON-FLARING PLASMAS IN ACTIVE REGION CORES II. NANOFLARE TRAINS

W. T. BARNES¹, P. J. CARGILL^{2,3}, AND S. J. BRADSHAW¹

¹Department of Physics & Astronomy, Rice University, Houston, TX 77251-1892; will.t.barnes@rice.edu, stephen.bradshaw@rice.edu

²Space and Atmospheric Physics, The Blackett Laboratory, Imperial College, London SW7 2BW; p.cargill@imperial.ac.uk

³School of Mathematics and Statistics, University of St Andrews, St Andrews, Scotland KY16 9SS

ABSTRACT

Despite its prediction over two decades ago, the detection of faint, high-temperature (“hot”) emission due to nanoflare heating in non-flaring active region cores has proved challenging. Using an efficient two-fluid hydrodynamic model, this paper investigates the properties of the emission expected from repeating nanoflares (a nanoflare train) of varying frequency as well as the separate heating of electrons and ions. If the emission measure distribution (EM(T)) peaks at $T = T_m$, we find that EM(T_m) is independent of details of the nanoflare train, and EM(T) above and below T_m reflects different aspects of the heating. Below T_m the main influence is the relationship of the waiting time between successive nanoflares to the nanoflare energy. Above T_m power-law nanoflare distributions lead to an extensive plasma population not present in a monoenergetic train. Furthermore, in some cases characteristic features are present in EM(T). Such details may be detectable given adequate spectral resolution and a good knowledge of the relevant atomic physics. In the absence of such resolution we propose some metrics that can be used to infer the presence of “hot” plasma.

Keywords: Sun:corona, Sun:nanoflares, plasmas, hydrodynamics

1. INTRODUCTION

The concept of heating the solar corona by nanoflares, first proposed by Parker (1988), has been developed extensively over the past two decades (e.g. Cargill 1994; Cargill & Klimchuk 2004; Klimchuk 2006). The term *nanoflare* has now become synonymous with impulsive heating in the energy range $10^{24} - 10^{27}$ erg, with no specific assumption regarding the underlying physical mechanism (for example, small-scale magnetic reconnection or hydromagnetic wave dissipation). In active region (AR) cores such as those we discuss in this paper, one strategy for constraining potential heating models is the analysis of the emission measure distribution as a function of temperature, $EM(T) = \int n^2 dh$. Cargill (1994); Cargill & Klimchuk (2004) predicted that EM(T) resulting from nanoflare heating should be wide, with a maximum value at $T = T_m \sim 10^{6.5}$ K and have a faint, high-temperature (8-10 MK) component. Below T_m , there is a scaling $EM(T) \sim T^a$ over a temperature range $10^6 \lesssim T \lesssim T_m$, a result first discussed by Jordan (1975). Observations from instruments onboard the Solar Dynamics Observatory (SDO, Pesnell et al. 2012) and *Hinode* spacecraft (Kosugi et al. 2007) have shown that $2 \lesssim a \lesssim 5$, with $T_m \approx 10^{6.5-6.6}$ (Warren et al. 2011, 2012; Winebarger et al. 2011; Tripathi et al. 2011; Schmelz & Pathak 2012; Del Zanna et al. 2015).

The emission component above T_m has been the subject of less study, but is likely to be important as the so-called “smoking gun” of nanoflare heating since its properties may bear a close link to the actual heating. While many workers (Reale et al. 2009; Schmelz et al. 2009; Miceli et al. 2012; Testa & Reale 2012; Del Zanna & Mason 2014; Petralia et al. 2014; Schmelz et al. 2015) have claimed evidence of this hot, faint component of the emission measure, poor spectral resolution (Testa et al. 2011; Winebarger et al. 2012) and non-equilibrium ionization (Bradshaw & Cargill 2006; Reale & Orlando 2008) may make a positive detection of nanoflare heating difficult. However, Brosius et al. (2014) used observations from the *EUNIS-13* sounding rocket to identify relatively faint emission from Fe XIX in a non-flaring active region (AR), suggesting temperatures of ~ 8.9 MK.

A scaling has been claimed for hot emission with $T > T_m$ such that $EM \propto T^{-b}$, with $b > 0$. This fit is usually done in the range $T_m \lesssim T \lesssim 10^{7.2}$. However, measured values of these “hotward” slopes are poorly constrained due to both the low magnitude of emission and the lack of available spectroscopic data in this temperature range (Winebarger et al. 2012). Warren et al. (2012) find $7 \lesssim b \lesssim 10$ with uncertainties of $\pm 2.5 - 3$, for 15 AR cores though Del Zanna &

Mason (2014), using observations from the Solar Maximum Mission, claim larger values for b . It must be noted though that reconstructing $EM(T)$ from spectroscopic and narrow-band observations is non-trivial, with different inversion methods often giving significantly different results (Landi et al. 2012; Guennou et al. 2013).

An important parameter for any proposed coronal heating mechanism is the frequency of energy release along a single magnetic strand, where the observed loop comprises many such strands. Nanoflare heating can be classified as being either a *high-* or *low-frequency*. In the case of high-frequency (HF) heating, t_N , the time between successive events, is such that $t_N \ll \tau_{cool}$, where τ_{cool} is a characteristic loop cooling time, and in the case of low-frequency (LF) heating $t_N \gg \tau_{cool}$ (Mulu-Moore et al. 2011; Warren et al. 2011; Bradshaw et al. 2012; Reep et al. 2013; Cargill et al. 2015). Steady heating is just high-frequency heating in the limit $t_N \rightarrow 0$. While a determination of t_N is of great importance, its measurement is challenging. For example, while direct observations of possible reconnection-associated heating through short timescale changes in loop structure and emission is feasible, as demonstrated by the Hi-C rocket flight (Cirtain et al. 2013; Cargill 2013), longer duration observations are required to constrain t_N . The previously-mentioned difficulties in reconstructing $EM(T)$ must also be borne in mind. Efforts to measure the heating frequency using narrow-band observations of intensity fluctuations in AR cores have proved similarly difficult (Ugarte-Urra & Warren 2014).

The use of hydrodynamic loop models, combined with sophisticated forward modeling, is a useful method for assessing a wide variety of heating scenarios. Such models of nanoflare-heated loops have found emission measure slopes consistent with those derived from observations in the temperature range $T < T_m$. For example, while Bradshaw et al. (2012) found that the full range of a could not be accounted for with low-frequency nanoflares, Reep et al. (2013) showed that using a tapered nanoflare train allowed for $0.9 \lesssim a \lesssim 4.5$. Cargill (2014), using a 0D loop model, investigated a large range of heating frequencies, $250 \leq t_N \leq 5000$ s, and found that only when t_N was between a few hundred and 2000 seconds and proportional to the nanoflare energy could the full range of observed emission measure slopes be found.

An analogous approach can be used to investigate the properties of the “hot” coronal component expected from nanoflare heating, and is the subject of the present series of papers. In Barnes et al. (2016) (Paper I, hereafter), we looked at the hot plasma properties due to a single isolated nanoflare. The effects of heating pulse duration, changes to conductive cooling due to heat flux limiting, differential heating of electrons and ions, and non-equilibrium ionization (NEI) were studied. It was shown that signatures of nanoflare heating are likely to be found in the temperature range $4 \lesssim T \lesssim 10$ MK. The prospect of measurable signatures above 10 MK was found to be diminished for short heating pulses (with duration < 100 s), NEI, and differential heating of the ions rather than the electrons. It is important to stress for a single nanoflare that while the “hot” plasma is present, it cannot actually be detected.

Single nanoflare are a good proxy for the LF heating scenario, but a study of nanoflare heating over a range of heating frequencies requires that we consider a “train” of nanoflares along a magnetic strand (Viall & Klimchuk 2011; Warren et al. 2011; Reep et al. 2013; Cargill et al. 2015). In this paper, we use an efficient two-fluid hydrodynamic model to explore the effect of a nanoflare train with varying t_N on $EM(T)$, in particular for $T > T_m$. Preferential species heating, NEI, power-law nanoflare distributions, and the effects of a variable t_N between events are considered and an emission measure ratio metric, similar to that discussed in Brosius et al. (2014), is used to characterize the various results. Section 2 discusses the numerical model we have used to conduct this study and the parameter space we have investigated. Section 3 shows the resulting emission measure distributions and diagnostics for the entire parameter space. Finally, Section 4 discusses how our results may be interpreted in the broader context of nanoflare heating and provides some concluding comments on our findings.

2. METHODOLOGY

2.1. Numerical Model

Hydrodynamic models are excellent tools for computing field-aligned quantities in coronal loops. However, because of the small cell sizes needed to resolve the transition region and consequently small timesteps demanded by thermal conduction, the use of such models in large parameter space explorations is made impractical by long computational runtimes (Bradshaw & Cargill 2013). We use the popular 0D enthalpy-based thermal evolution of loops (EBTEL) model (Klimchuk et al. 2008; Cargill et al. 2012a,b, 2015) in order to efficiently simulate the evolution of a coronal loop over a large parameter space. This model, which has been successfully benchmarked against the 1D hydrodynamic HYDRAD code of Bradshaw & Cargill (2013), computes, with very low computational overhead, time-dependent, spatially-averaged loop quantities.

In order to treat the evolution of the electron and ion populations separately, we use a modified version of the usual

EBTEL equations. This amounts to computing spatial averages of the two-fluid hydrodynamic equations over both the transition region and corona. A full description and derivation of these equations can be found in the appendix of [Paper I](#). The relevant two-fluid pressure and density equations are,

$$\frac{d}{dt}\bar{p}_e = \frac{\gamma-1}{L} [\psi_{TR} - (\mathcal{R}_{TR} + \mathcal{R}_C)] + k_B \bar{n} \nu_{ei} (\bar{T}_i - \bar{T}_e) + (\gamma-1)\bar{Q}_e, \quad (1)$$

$$\frac{d}{dt}\bar{p}_i = -\frac{\gamma-1}{L} \psi_{TR} + k_B \bar{n} \nu_{ei} (\bar{T}_e - \bar{T}_i) + (\gamma-1)\bar{Q}_i, \quad (2)$$

$$\frac{d}{dt}\bar{n} = \frac{c_2(\gamma-1)}{c_3\gamma L k_B \bar{T}_e} (\psi_{TR} - F_{ce,0} - \mathcal{R}_{TR}), \quad (3)$$

where $c_2 = \bar{T}_e/T_{e,a} \approx 0.9$, $c_3 = T_{e,0}/T_{e,a} \approx 0.6$, ν_{ei} is the electron-ion binary Coulomb collision frequency, and ψ_{TR} is a term included to maintain charge and current and neutrality. Additionally, $c_1 = \mathcal{R}_{TR}/\mathcal{R}_C$ and its formulation is discussed in [Cargill et al. \(2012a\)](#) with additional modifications detailed in Appendix 1 of [Paper I](#). These equations are closed by the equations of state $p_e = k_B n T_e$ and $p_i = k_B n T_i$. In the cases where we treat the plasma as a single-fluid, we use the original EBTEL model as described in [Klimchuk et al. \(2008\)](#); [Cargill et al. \(2012a\)](#).

The loop is heated by a prescribed heating function, applied to either the electrons (\bar{Q}_e) or the ions (\bar{Q}_i). Both species cool through a combination of thermal conduction ($F_{ce,0}$, $F_{ci,0}$) and an enthalpy flux to the lower atmosphere, with the electrons also undergoing radiative cooling (\mathcal{R}_C). In the case of conductive cooling, a flux limiter, $F_s = (1/2) f n k_B T V_e$, is imposed to mitigate runaway cooling in a low-density, high-temperature plasma. In all cases we use a saturation limit of $f = 1$. See [Paper I](#) for a discussion of how f is likely to effect the presence of hot emission in a nanoflare-heated plasma.

2.2. Energy Budget

We define our heating function in terms of a series of discrete heating events plus a static background heating to ensure that the loop does not drop to unphysically low temperatures and densities between events. For a triangular heating pulse of duration τ injected into a loop of half-length L and cross-sectional area A , the total event energy is $\varepsilon = LAH\tau/2$, where H is the heating rate. Each model run will consist of N heating events, each with peak amplitude H_i , and a steady background heating of $H_{bg} = 3.5 \times 10^{-5} \text{ erg cm}^{-3} \text{ s}^{-1}$.

Recent observations have suggested that loops in AR cores are maintained at an equilibrium temperature of $T_m \approx 4$ MK ([Warren et al. 2011, 2012](#)). Using our modified two-fluid EBTEL model, we have estimated the time-averaged volumetric heating rate needed to keep a loop of half-length $L = 40$ Mm at $\bar{T} \approx 4$ MK as $H_{eq} \sim 3.6 \times 10^{-3}$. In the single-fluid EBTEL model, this value is slightly lower because losses due to electron-ion collisions are ignored. Thus, to maintain an emission measure peaked about T_m , for triangular pulses, the individual event heating rates are constrained by,

$$H_{eq} = \frac{1}{t_{total}} \sum_{i=1}^N \int_{t_i}^{t_i+\tau} dt Q(t) = \frac{\tau}{2t_{total}} \sum_{i=1}^N H_i, \quad (4)$$

where t_{total} is the total simulation time. Note that if $H_i = H_0$ for all i , the heating rate for each event is $H_i = H_0 = 2t_{total}H_{eq}/N\tau$. Thus, for $L = 40$ Mm, $A = 10^{14} \text{ cm}^2$, the average energy per event for a loop heated by $N = 20$ nanoflares in $t_{total} = 8 \times 10^4 \text{ s}$ is $\varepsilon = LA t_{total} H_{eq}/N \approx 5.8 \times 10^{24} \text{ erg}$.

We define the heating frequency in terms of the waiting time, t_N , between successive heating events. Following [Cargill \(2014\)](#), the range of waiting times is $250 \leq t_N \leq 5000 \text{ s}$ in increments of 250 s, for a total of 20 different possible heating frequencies. Additionally, t_N can be written as $t_N = (t_{total} - N\tau)/N$, where we fix $t_{total} = 8 \times 10^4 \text{ s}$ and $\tau = 200 \text{ s}$. Note that because t_{total} and τ are fixed, as t_N increases, N decreases. Correspondingly, $\varepsilon_i = LA\tau H_i/2$, the energy injected per event, increases according to [Equation 4](#) such that the total energy injected per run is constant.

According to the nanoflare heating model of [Parker \(1988\)](#), turbulent loop footpoint motions twist and stress the field, leading to a buildup and subsequent release of energy. Following [Cargill \(2014\)](#), we let $\varepsilon_i \propto t_{N,i}^\beta$, where ε_i , $t_{N,i}$ are the total energy of event i and waiting time following event i , respectively, and $\beta = 1$ such that the event energy scales linearly with the waiting time. The reasoning for such an expression is as follows. Bursty, nanoflare heating is thought to arise from the stressing and subsequent relaxation of the coronal field. If a sufficient amount of energy is released into the loop, the field will need enough time to “wind up” again before the next event such that the subsequent waiting time is large. Conversely, if only a small amount of energy is released, the field will require a shorter re-winding time, resulting in a shorter interval between the subsequent events. Thus, this scaling provides a way to incorporate a more

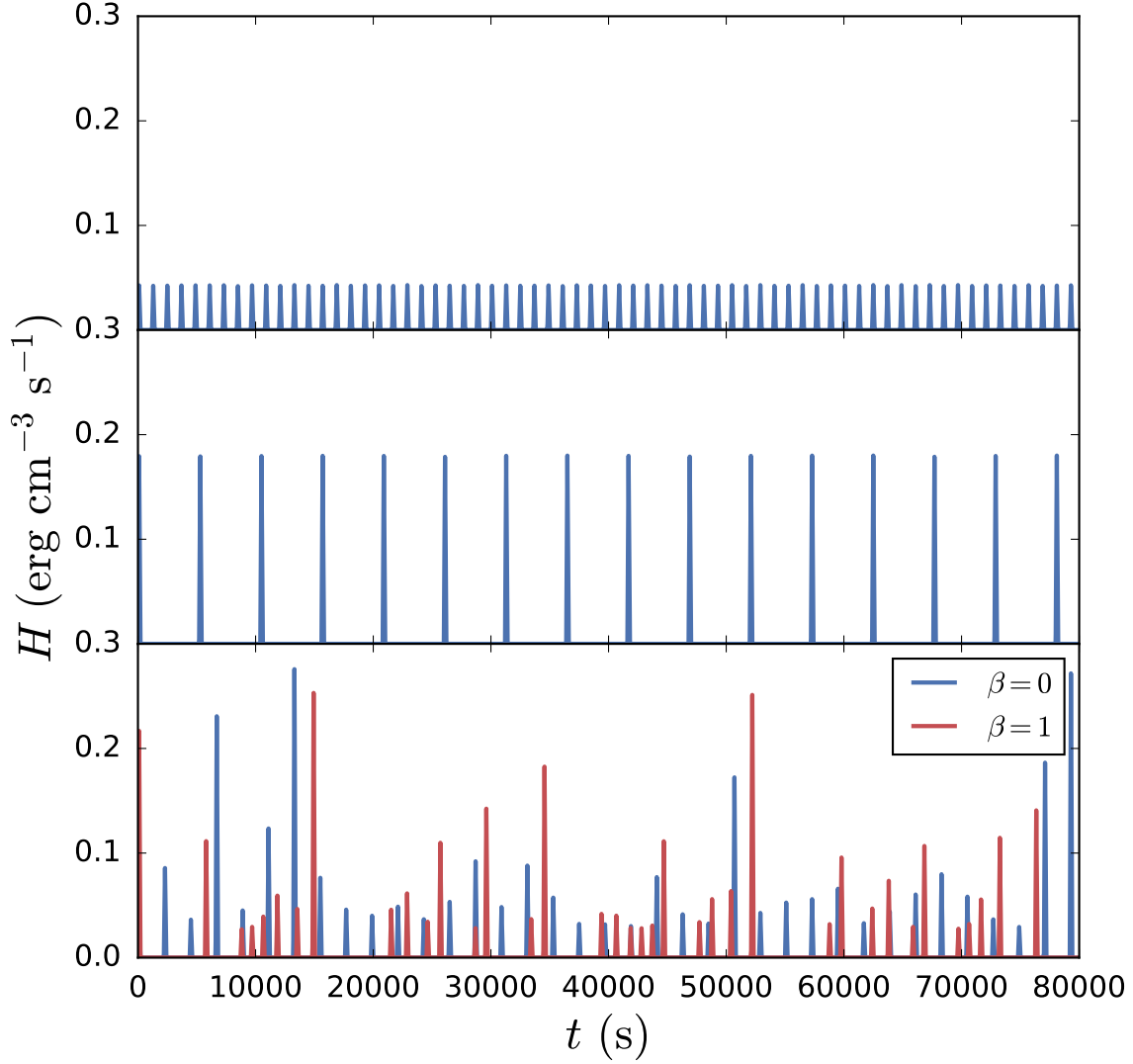


Figure 1. Examples of four different heating functions: uniform heating amplitudes for $t_N = 1000$ s (top), uniform heating amplitudes for $t_N = 5000$ s (middle), and heating amplitudes drawn from a power-law distribution with index $\alpha = -1.5$ (bottom). In the bottom panel, the events shown in red have waiting times that depend on the previous event energy while the events shown in blue have uniform waiting times. The average waiting time in both cases is $t_N = 2000$ s.

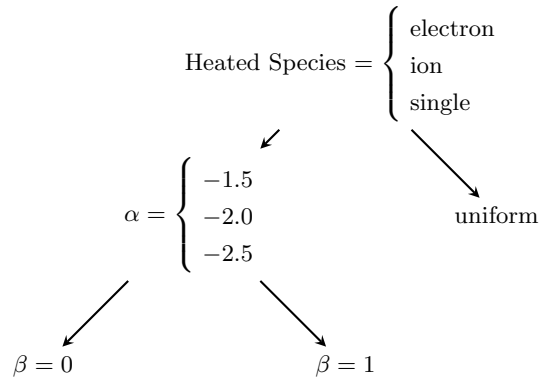


Figure 2. Total Parameter space covered. “single” indicates a single-fluid model. α is the power-law index and β indicates the scaling in the relationship $\varepsilon \propto T_N^\beta$, where $\beta = 0$ corresponds to the case where t_N and the event energy are independent. Note that $(3 \alpha \text{ values}) \times (2 \beta \text{ values}) + \text{uniform heating} = 7$ different types of heating functions per heated species.

physically motivated heating function into a hydrodynamic model which cannot self-consistently determine the heat input based on the evolving magnetic field. Figure 1 shows the various heating functions used for several example t_N values. Note that when $\beta = 1$, t_N is the *average* waiting time between events since the waiting time after a particular event i is dependent on the energy of that event.

2.3. Heating Statistics

We compute the peak heating rate per event in two different ways: 1) the heating rate is uniform such that $H_i = H_0$ for all i and 2) H_i is chosen from a power-law distribution with index α where $\alpha = -1.5, -2.0$, or -2.5 . For the second case, it should be noted that, when $t_N \approx 5000$ s, $N \sim 16$ events, meaning the events from a single run do not accurately represent the distribution of index α . Thus, a sufficiently large number of runs, N_R , are computed for each t_N to ensure that the total number of events is $N_{tot} = N \times N_R \sim 10^4$ such that the distribution is well-represented. Figure 2 shows the parameter space we will explore. For each set of parameters and waiting time t_N , we compute the resulting emission measure distribution for N events in a period t_{total} . This procedure is repeated N_R times until $N \times N_R \sim 10^4$ is satisfied. Thus, when $t_N = 5000$ s and $N \sim 16$, $N_R = 625$, meaning the model is run 625 times with a waiting time of $t_N = 5000$ s in order to properly fill out the event energy distribution.

2.4. Non-equilibrium Ionization

When considering the role of nanoflares in the production of hot plasma in AR cores, it is important to take non-equilibrium ionization (NEI) into account (Bradshaw & Cargill 2006; Reale & Orlando 2008; Barnes et al. 2016). In a steady heating scenario, the ionization state is an adequate measure of the electron plasma temperature. Because the heating timescale is long (effectively infinite), the ionization state has plenty of time to come into equilibrium with the electron temperature.

In a nanoflare train, when the heating frequency is high, the loop is not allowed to drain or cool sufficiently between events, meaning the ionization state is kept at or near equilibrium. However, as the heating frequency decreases, the loop is allowed to cool and drain more and more during the inter-event period. If the heating occurs on a short enough timescale, the ionization state will not be able to reach equilibrium with the electron plasma before the loop undergoes rapid cooling by thermal conduction. Furthermore, if the frequency is sufficiently low so as to allow the loop to drain during the inter-event period, the ionization equilibrium timescale will increase. Thus, in the context of intermediate- to low-frequency nanoflares, NEI should be considered.

As in Paper I, we use the numerical code¹ outlined in Bradshaw (2009) to asses the impact of NEI on our results. Given a temperature ($T(t)$) and density ($n(t)$) profile from EBTEL, we compute the non-equilibrium ionization states for Fe IX through XXVII and the corresponding effective electron temperature, T_{eff} , that would be inferred by assuming ionization equilibrium. Using T_{eff} , we are then able to compute a corresponding NEI emission measure distribution, $EM(T_{eff})$.

3. RESULTS

We now show the results of our nanoflare train simulations for each point in our multidimensional parameter space: species heated (single-fluid, electron or ion), power-law index (α), waiting time (t_N), and waiting-time/event energy relationship (β). In each 0D hydrodynamic simulation, a loop of half-length $L = 40$ Mm is heated by N triangular events of duration $\tau = 200$ s and peak heating rate H_i for a duration of $t_{total} = 8 \times 10^4$ s. The average interval between subsequent events is t_N (in the uniform and $\beta = 0$ cases, $t_{N,i} = t_N$ exactly for all i). We focus primarily on the emission measure distribution, $EM(T)$, and observables typically calculated from $EM(T)$. In all cases, the coronal emission measure is calculated according to the method outlined in section 3 of Paper I. The corresponding NEI results, $EM(T_{eff})$, are calculated similarly, but using T_{eff} (see Subsection 2.4) instead of T . All results were processed using the IPython system for interactive scientific computing in Python (Pérez & Granger 2007) as well as the NumPy and Scipy numerical and scientific Python libraries (van der Walt et al. 2011). All results were visualized using the matplotlib graphics library (Hunter 2007).

3.1. Emission Measure Distributions

We compare $EM(T)$ for three different types of heating functions, across a sample of six different heating frequencies. Figure 3, Figure 4, and Figure 5 show the emission measure distributions for the single-fluid, electron heating, and ion

¹ This code has been made freely available by the author and can be downloaded at: <https://github.com/rice-solar-physics/IonPopSolver>.

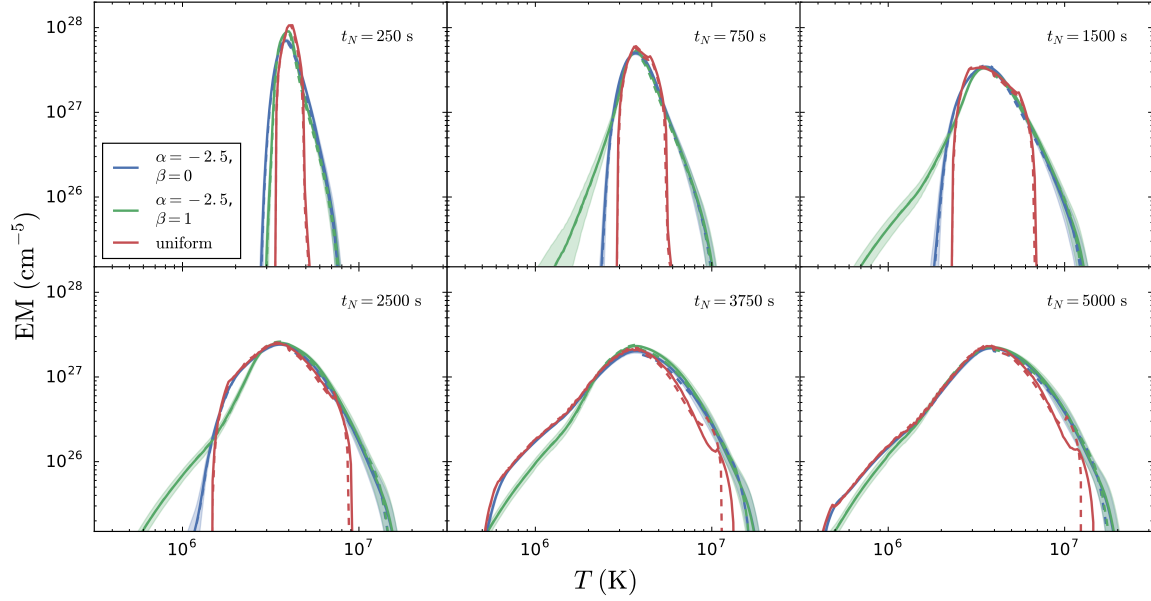


Figure 3. Emission measure distributions for waiting times $t_N = 250, 750, 1500, 2500, 3750, 5000$ s in the single-fluid case. The three types of heating functions shown are uniform heating rates (red), heating rates chosen from a power-law distribution of $\alpha = -2.5$ where the waiting time after each event is proportional to the heating rate of the event (green). For the last case ($\beta = 1$), t_N is the average waiting time for all events. Note that in some panels, the blue $\beta = 0$ curves may not be visible because they overlap heavily with the green $\beta = 1$ curves. The solid lines in the two power law cases show the mean $EM(T)$ over N_R runs and the shading indicates 1σ from the mean. The dashed lines denote the corresponding $EM(T_{eff})$ distribution. The standard deviation is not included in the NEI results.

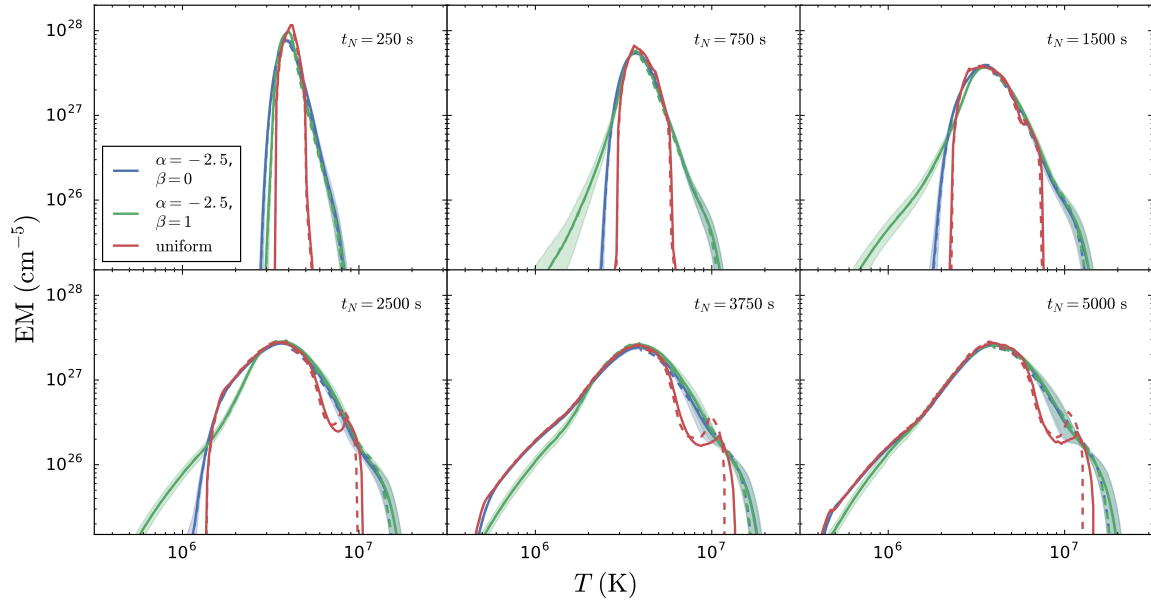


Figure 4. Same as Figure 3, but for the case where only the electrons are heated.

heating cases respectively. Each panel corresponds to a different average waiting time (t_N) and includes three different types of heating functions: uniform heating events (red), events chosen from a single power-law distribution of index $\alpha = -2.5$ with constant waiting time ($\beta = 0$ case, blue), and a waiting time that depends on the energy released in the preceding event ($\beta = 1$ case, green). The dashed lines denote the corresponding NEI cases, $EM(T_{eff})$. The cases shown in Paper I correspond approximately to the red curves in the lower right panels ($t_N = 5000$ s) in each of the three figures since the loop is allowed to cool and drain completely before reheating and a single nanoflare energy is used.

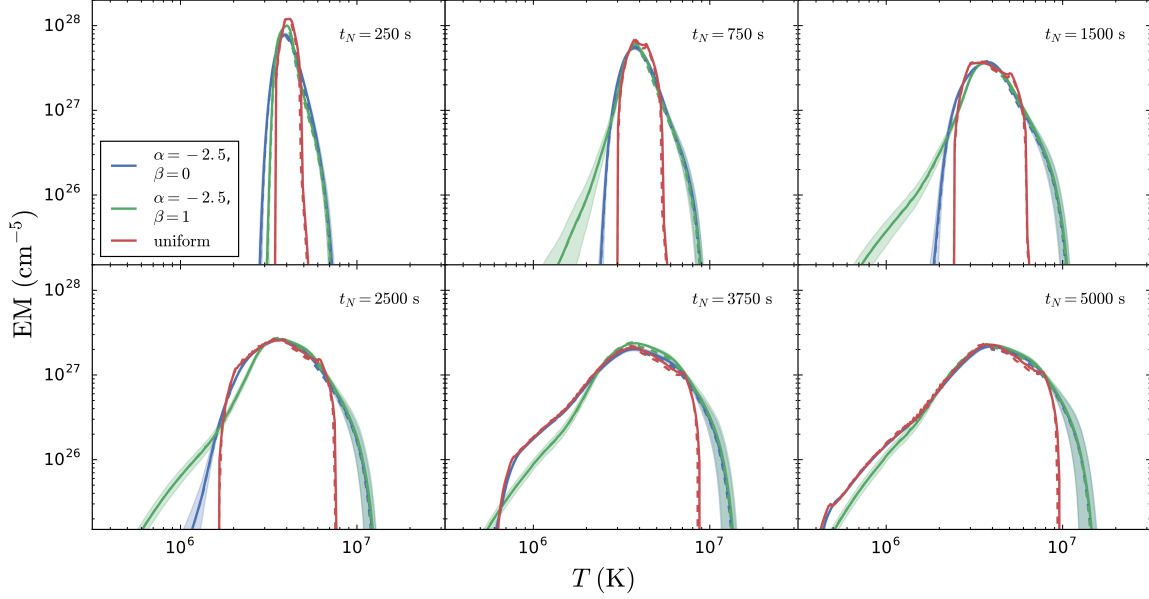


Figure 5. Same as Figure 3, but for the case where only the ions are heated.

In Subsection 2.3, we noted that for heating functions using a power-law energy distribution, for each t_N , we run the model N_R times. Thus, for each point in our parameter space, we produce N_R $EM(T)$ curves. In order to present our results compactly, the solid lines in Figure 3, Figure 4, and Figure 5 each show the mean $EM(T)$ over all N_R curves. The shading represents 1σ from the mean. In this way, we account for the variations that may occur because of a lack/excess of strong heating events due to limited sampling from the power-law distribution of possible heating rates.

In all cases, $EM(T)$ has some generic properties. Firstly, as expected from Cargill (2014), as t_N increases, $EM(T)$ widens, extending to both cooler (< 4 MK) and hotter (> 4 MK) temperatures. Secondly, for a prescribed value of t_N , the values of $EM(T_m)$ and T_m are approximately the same for all forms of heating. This can be attributed to the effective coupling between the species at $n(T_m)$ and suggests that $EM(T)$ above and below T_m can be considered separately, with each providing information about different aspects of the heating.

For $T < T_m$, the extension of $EM(T)$ toward cooler temperatures arises because as t_N increases there is more time between successive heating events so that the loop cools to lower temperatures before being reheated. The dependence on α and β is similar to that described in Cargill (2014). For both uniform heating (red) and a power-law index without waiting time (blue), $EM(T)$ falls off more rapidly than when a waiting time is included (green) for intermediate frequencies. For example, for $t_N = 1500$ s, both the uniform and $\beta = 0$ cases show little to no emission below 2 MK while the $\beta = 1$ case extends to temperatures well below 1 MK. Thus this part of $EM(T)$ has information about the need for a waiting time, but not about the details of which species is heated.

The behavior of $EM(T)$ above T_m is more complicated, but because $EM(T_m)$ and T_m are the same for all parameters, we can make a meaningful comparison between the different heating models. For the single-fluid model and short t_N , the emission measure distribution falls off sharply on the hot side for a uniform nanoflare train, but choosing heating events from a power law leads to a broader distribution. This just reflects the different initial temperatures generated with a power-law distribution since $T \simeq H^{2/7}$, where H is the heating rate. As t_N increases, the distribution for uniform heating gradually broadens as the initial temperature rises due to the lower density in which the heating occurs. A similar broadening occurs for power law heating distributions with the $\beta = 0$ and $\beta = 1$ results showing little difference. Note that the $\beta = 0$ curve is barely visible as it overlaps almost completely with the $\beta = 1$ curve. Especially interesting in this case are the results with NEI included. For a uniform nanoflare train, NEI plays no role up to $t_N = 2500$ sec, but above that it restricts the temperatures that can be detected, as shown in Paper I. This hot emission is relocated to cooler temperatures, resulting in a small “bump” in the emission measure distribution near 10 MK. On the other hand, NEI plays almost no role in the power-law distributions, for either the $\beta = 0$ or $\beta = 1$ cases.

For electron heating, the $EM(T)$ curves for the different types of heating functions shown in Figure 4 evolve similarly to those shown in Figure 3. For $t_N \leq 750$ s, the electron and single-fluid cases are quite similar at $T > T_m$. However, for $t_N \geq 1500$ s $EM(T)$ steepens just above 4 MK and then flattens out near 10 MK. This change in shape is most obvious in the uniform heating case where a distinct “hot shoulder” forms just above 10 MK. In the power law cases, this

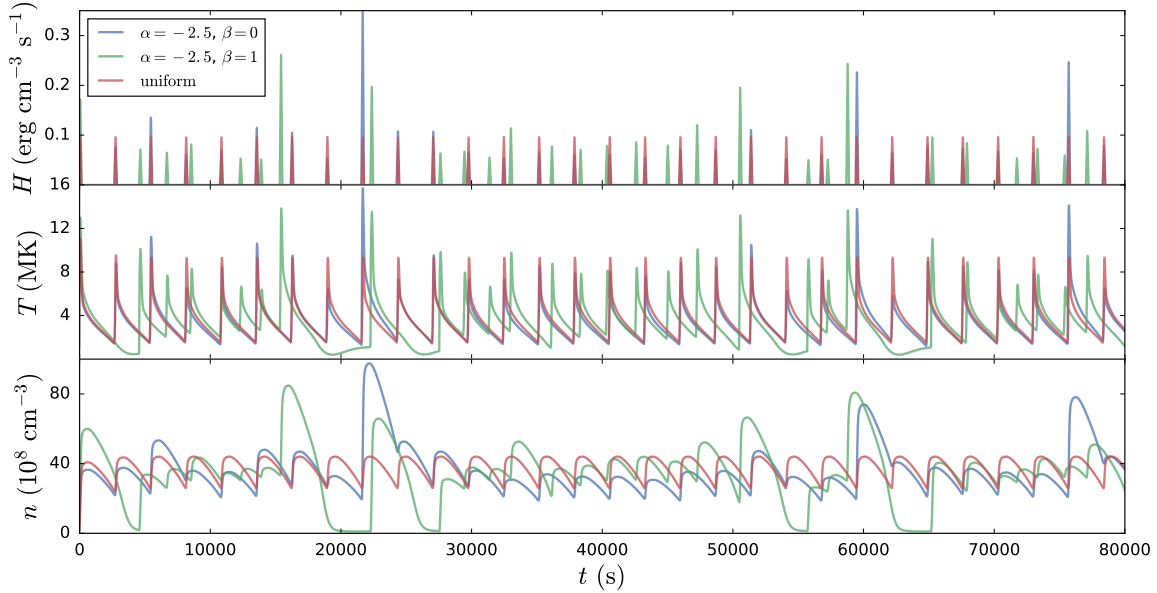


Figure 6. Example heating (top), temperature (middle), and density (bottom) profiles for the case in which only the electrons are heated with a waiting time of $t_N = 2500$ s (i.e. an intermediate heating frequency). The three curves shown in each panel correspond to uniform heating rates (red), heating rates chosen from a power-law distribution of $\alpha = -2.5$ (blue), and heating rates chosen from a power-law distribution of $\alpha = -2.5$ where the time between successive events is proportional to the heating rate of the preceding event (green).

feature is less pronounced though $EM(T)$ extends to slightly higher temperatures. Again for a power-law distribution NEI is not important while for uniform heating, the hot emission is again truncated and leads to a “bump” in $EM(T)$ near 10 MK.

When only the ions are heated (Figure 5), for intermediate to low heating frequencies (i.e. $t_N \geq 1500$ s), $EM(T)$ in the uniform heating case is truncated below 10 MK and in the power law cases extends to just above 10 MK for the longest waiting time ($t_N = 5000$ s). This cutoff at lower temperatures is due to the fact that the electrons cannot “see” the ions until they have cooled well below their peak temperature. This is discussed in Paper I though in the single-pulse cases, the cutoff occurred at lower temperatures. Additionally, in both the uniform and power law cases, the peak of $EM(T)$ is wider for these low frequencies compared to those shown in the lower right panels of Figure 3 and Figure 4. NEI now plays no role in any of the cases.

From these results, we see that new information about the heating is potentially available above T_m , but unlike at lower temperatures (i.e. $T < T_m$), information about the role of a waiting time is lost. For high frequency nanoflares, there is no plasma above $10^{6.8}$ K in any of the heating scenarios. For intermediate heating frequencies, there is a significant enhancement in $EM(T > T_m)$ for the power law cases relative to the uniform heating case in the single-fluid, electron heating, and ion heating cases. For low frequencies, this discrepancy is less pronounced, though the uniform single-fluid and electron heating cases show distinctive features in $EM(T)$ near 10 MK.

3.2. Pre-nanoflare Density

In Cargill (2014), Paper I, and Subsection 3.1, we have suggested that the plasma density prior to the nanoflare occurring is a crucial parameter in determining the emission measure distribution. This arises in two distinct ways. Below T_m , the temperature and density at which the nanoflare occurs cuts off the emission at lower temperatures. When combined with an energy-dependent waiting time, this can lead to a range of EM slopes in this region (Cargill 2014). Above T_m , the initial density determines the temperature increase due to the nanoflare, how quickly the initial hot plasma cools, and whether NEI effects are important. We now examine this further.

In the single-fluid and electron heating cases, while $EM(T)$ in the uniform and power-law heating cases generally agree for low-frequency heating ($t_N = 5000$ s), for intermediate frequencies ($t_N \approx 750 - 2500$ s), the power law cases show an enhanced high-temperature component compared to the uniform case as seen in Figure 3 and Figure 4. Figure 6 shows sample heating, temperature, and density profiles for an intermediate heating frequency (i.e. a waiting time of $t_N = 2500$ s), in the case where only the electrons are heated, for the three different types of heating functions. In the uniform heating rate case (red), each event has a maximum heating rate of H_0 such that the loop undergoes

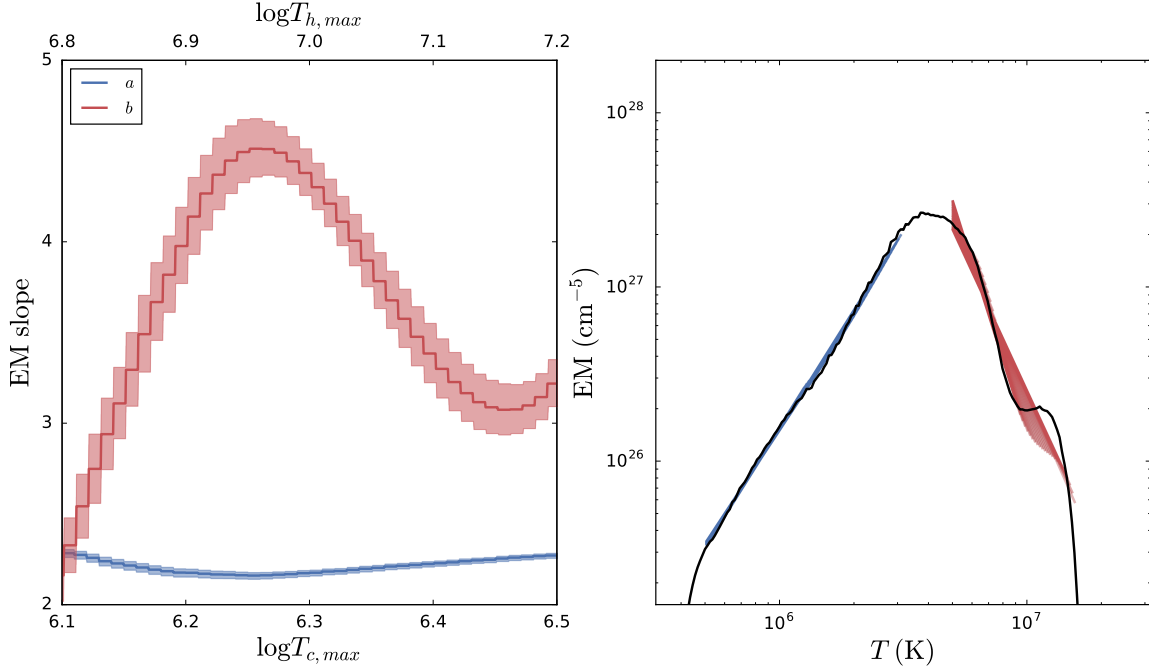


Figure 7. Fits to a sample emission measure distribution constructed from a loop plasma in which only the electrons were heated by events chosen from a power-law distribution with $\alpha = -2.5$ and equally spaced by an interval of $t_N = 5000$ s. **Left:** $EM(T)$ slope as a function of upper bound on fit interval for both the hot (red) and cool (blue) side of $EM(T)$. The shading denotes the uncertainty of the fit. The bottom axis corresponds to the varying upper limit on the fit to the cool side while the top axis corresponds to the varying upper limit on the fit to the hot side. **Right:** $EM(T)$ with the overlaid hot (red) and cool (blue) fit lines whose slopes correspond to those shown on the left. The cool power-law fits describe $EM(T)$ for $T < 4$ MK quite well while a similar fit on the hot side fails to accurately describe the shape of the emission measure distribution for $T > 4$ MK.

$N \approx 30$ identical heating and cooling cycles, each time reaching a maximum temperature and density of $T_{max,0}$ and $n_{max,0}$, respectively.

In comparing various heating models, we insist that the total energy injected into the loop is the same for each run (see Equation 4). When the nanoflare heating rates are distributed according to a power law, there will be many events where $H_i < H_0$ and a few events where $H_i \gg H_0$. These few high energy events lead to $T \gg T_{max,0}$ (blue and green curves) as seen in the middle panel of Figure 6. Because these events are injected into a plasma that is sufficiently dense due to the draining and cooling times being longer than the time since the previous event, the emission measure is able to “see” these hot temperatures, resulting in a > 10 MK component of $EM(T)$ (see lower left panel of Figure 3 and Figure 4). In the uniform case, $T_{max,0} < 10$ MK such that $EM(T)$ has a steep cutoff right at 10 MK.

3.3. Hot Plasma Diagnostics

The relation of these results to potential solar observations is made difficult by incomplete temperature coverage. For example, we noted earlier that the temperature coverage for *Hinode* and SDO is good for $T < T_m$, but patchy for $T > T_m$. On the other hand, the proposed MaGIXS (Kobayashi et al. 2011; Winebarger 2014) instrument has the opposite performance regime. This differs from EUVE observations of some stellar coronae which have very complete temperature coverage from 10^6 K to over 10^7 K (e.g. Sanz-Forcada et al. 2003), and have been modeled using low frequency nanoflares (Cargill & Klimchuk 2006). The results in Subsection 3.1 suggest that given good spectral resolution, there may be detectable features in $EM(T)$, although atomic physics and other uncertainties would still be a concern. Instead, in the following sub-sections we propose ways that the paucity of solar temperature coverage can be partially remedied by a consideration of simple metrics.

3.3.1. Emission Measure Slope

As we discussed in the Section 1, a commonly-used observable is the emission measure slope a such that $EM \propto T^a$ for $10^{5.5} \leq T \leq 10^{6.6}$ K. Both observational and modeling studies have found that $2 \lesssim a \lesssim 5$ (see Table 3 of Bradshaw et al. 2012) and in particular, Cargill (2014) found that a heating function of the form $t_N \propto \varepsilon$ was needed in order to account for this range of slopes. In this range, the EIS instrument (Culhane et al. 2007) on *Hinode* permits good temperature coverage. Additionally, a similar scaling of $EM \propto T^{-b}$ for $10^{6.6} \leq T \leq 10^{7.0}$ has been claimed though

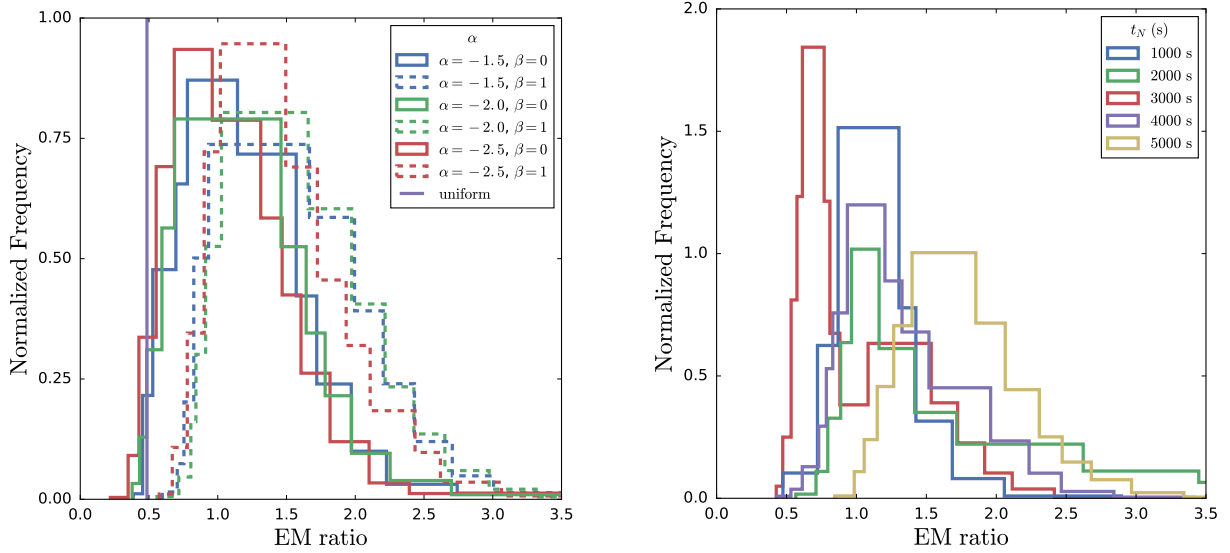


Figure 8. Histograms of emission measure ratios $\text{EM}(T_{\text{hot}})/\text{EM}(T_{\text{cool}})$, where $T_{\text{hot}} = 10^{6.95}$ K and $T_{\text{cool}} = 10^{6.2}$ K, for all heating function types and heating frequencies for the single fluid case. In both panels each histogram is normalized such that for each distribution $P(x)$, $\int_{-\infty}^{\infty} dx P(x) = 1$ and the bin widths are calculated using the Bayesian blocks method of Scargle et al. (2013) as implemented in the astroML Python package for statistical learning in astronomy (VanderPlas et al. 2012). **Left:** Emission measure ratios separated by heating function type for all heating frequencies, $250 \leq t_N \leq 5000$ s. Because there are too few (< 20) EM ratio measurements for the uniform case to construct a meaningful histogram, we denote the median of the uniform results with a vertical line, shown here in purple. **Right:** Emission measure ratios separated by waiting time, t_N . For aesthetic purposes, only five values of t_N are shown, $t_N = 1000, 2000, 3000, 4000, 5000$ s.

measurements of b have been subject to large uncertainties (Warren et al. 2012) due to intermittent temperature coverage.

Figure 7 shows an example of how both a and b can be calculated from the cool and hot sides of $\text{EM}(T)$, respectively. We select a single sample run from our parameter space in which only the electrons are heated by nanoflares from a power-law distribution of $\alpha = -2.5$ and spaced uniformly by an interval of $t_N = 5000$ s. We calculate the resulting $\text{EM}(T)$ and fit $\log \text{EM}$ to $a \log T$ on $\log T_{c,\min} < \log T < \log T_{c,\max}$ and $-b \log T$ on $\log T_{h,\min} < \log T < \log T_{h,\max}$ using the Levenburg-Marquardt algorithm for least-squares curve fitting. We fix the lower limit on each interval such that $T_{c,\min} = 10^{5.7}$ K and $T_{h,\min} = 10^{6.7}$ K and vary the upper limits over $10^{6.1} < T_{c,\max} < 10^{6.5}$ K and $10^{6.8} < T_{h,\max} < 10^{7.2}$ K. The left panel of Figure 7 shows a (blue) and b (red) as a function upper limit of the fit interval, $T_{c,\max}$ (bottom axis) and $T_{h,\max}$ (top axis), respectively. The shading denotes the uncertainty of the fit. The right panel of Figure 7 shows the resulting fit lines superimposed on the emission measure distribution.

From the left panel of Figure 7, we see that, while a is relatively insensitive to the fit interval, b varies between approximately 2 and 4.5 depending on the choice of bounds. Furthermore, the uncertainty in the fitting procedure for b is relatively large, with the average uncertainty over the entire range of $T_{h,\max}$ being $\bar{\sigma}_b \approx 0.17$. Contrastingly, we find that $a \approx 2.3$ with little variation over all values of $T_{c,\max}$ considered here and that $\bar{\sigma}_a \approx 0.018$, nearly an order of magnitude smaller than $\bar{\sigma}_b$. The overlaid fit lines in the right panel of Figure 7 similarly show that while $\log \text{EM}$ is roughly linear over $5.7 < \log T < 6.5$, this is not the case for the interval $6.7 < \log T < 7.2$. In particular, a function of the form T^{-b} cannot describe the hot shoulder in the emission measure distribution near $10^{7.1}$ K.

Our results here suggest that while a is an adequate parameter for describing the cool side of $\text{EM}(T)$, the functional form $\text{EM} \sim T^{-b}$ does not adequately capture the character of the hot part of $\text{EM}(T)$ over any reasonable temperature range. Antiochos & Sturrock (1978) showed analytically that accounting for evaporative cooling and assuming constant pressure gives $b = 11/2$, though this value can be as low as $b = 5/2$ if a flux limiter is included. However, in Paper I, we showed that in the case of a single 200 s nanoflare that heats only the electrons, the assumption of constant electron pressure during the heating and early conductive cooling phases does not hold. Our results here are consistent with our findings in Paper I in that the parameter b does not provide any valuable information about $\text{EM}(T)$ for $T > T_m$ when two-fluid effects are considered. Clearly, an alternative metric for measuring the amount of hot plasma in the emission measure distribution is needed.

3.3.2. Emission Measure Ratio

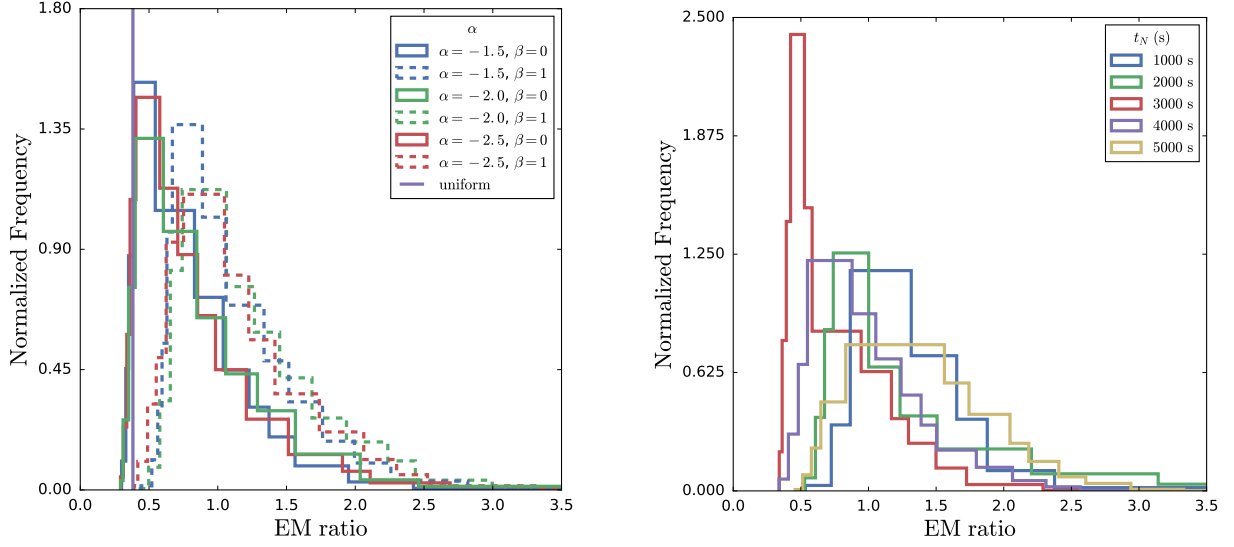


Figure 9. Same as Figure 8, but for the case where only the electrons are heated.

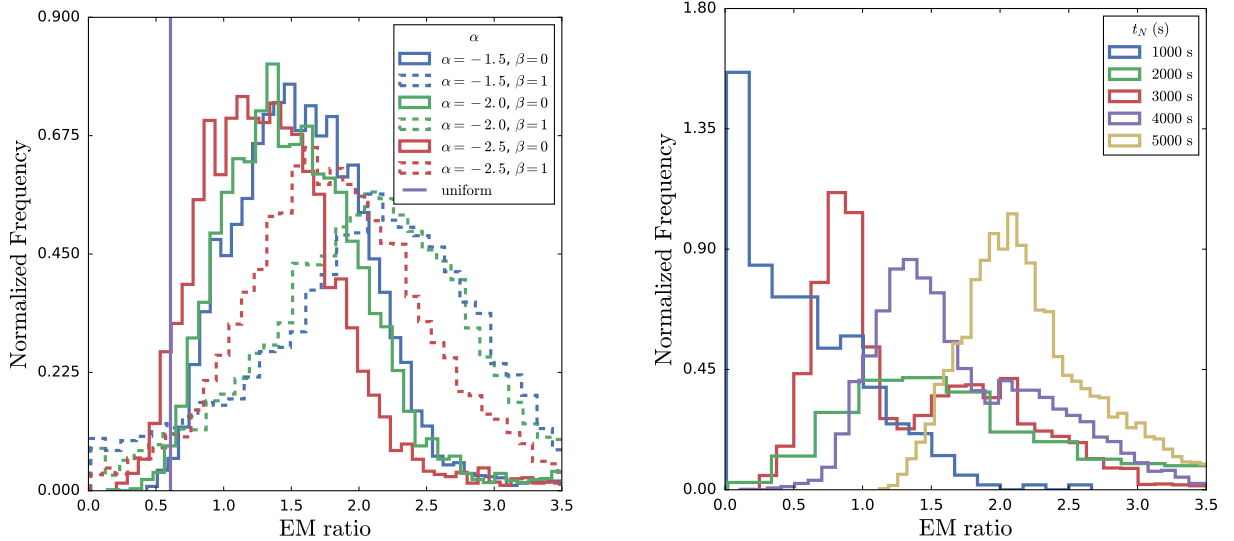


Figure 10. Same as Figure 8, but for the case where only the ions are heated. Here, the bin widths are calculated according to the well-known Freedman-Diaconis formula (Freedman & Diaconis 1981)

Brosius et al. (2014) proposed another possible diagnostic for the hot non-flaring corona. Using observations of an active region from the *EUNIS-13* sounding rocket, they found that the intensity ratio of Fe XIX (formed at $T \approx 10^{6.95}$ K) to Fe XII (formed at $T \approx 10^{6.2}$ K) is ~ 0.59 inside the AR core as compared to ~ 0.076 outside. They argue that this provides possible evidence for impulsive heating. This arises from the fact that the EM(T) distribution resulting from low- and intermediate-frequency nanoflares is dual-valued as a function of temperature (see Figure 3–Figure 5 and Cargill 1994): for example, in the lower right panel of Figure 3, $EM \approx 10^{26.5} \text{ cm}^{-5}$ at $T = 10^{6.2}$ K and $10^{6.9}$ K. This suggests that the approach of Brosius et al. (2014) could be used for any pair of appropriate emission lines and is likely to be of particular use where very limited spectral coverage is available either above or below T_m . Indeed for impulsive heating of any kind, the generic EM(T) curve remains similar (though not identical) as the magnitude of the heating changes. For flare-like energy release one would expect the hot emission to be much greater than the cold emission, with the opposite in the quiet Sun.

We define a general emission measure ratio, $EM(T_{hot})/EM(T_{cool})$ and for this paper consider $T_{hot} = 10^{6.95}$ K and $T_{cool} = 10^{6.2}$ K, consistent with Brosius et al. (2014). This also provides a way to compare in a concise way every point in our multidimensional parameter space though we acknowledge that we are reducing 8×10^4 s of loop evolution

to a single value. This ratio is shown in [Figure 8](#), [Figure 9](#), and [Figure 10](#) for the single-fluid model, electron and ion heating, respectively. In the left-hand panels each individual histogram (denoted by linestyle and color) corresponds to a different type of heating function. This means, for example, that the solid blue histogram includes emission measure ratios for all values of t_N , but for only those cases where heating events are chosen from a power-law distribution of $\alpha = -1.5$ and $t_{N,i} = t_N$ for all i (i.e. $\beta = 0$). The right panels show these same emission measure ratios, but now categorized by t_N . For example, the solid red histogram includes emission measure ratios for every type of heating function (i.e. uniform, all α and all β), but for only those runs where $t_N = 3000$ s. Note that we choose to only show results for five values of t_N for aesthetic purposes.

Considering first the left hand panels, in the single fluid model the ratio is largely insensitive to α and is peaked sharply at $\sim 0.75 - 1.0$ although the distribution peaks at slightly higher values for the $\beta = 1$ case (~ 1.25). Note that the uniform heating results (whose median is denoted by the vertical purple line near ~ 0.5) show emission measure ratios significantly less than those in the power law cases, consistent with the reduced hot emission shown in [Figure 3](#). For electron heating the ratio is again insensitive to α , but is narrower and falls off more quickly toward higher emission measure ratios. The $\beta = 0$ cases (for all α) peak near 0.5, with the $\beta = 1$ cases all peaking at slightly higher values, but all less than 1. For ion heating the $\beta = 0$ distributions peak at lower values compared to those with $\beta = 1$. Again the results are relatively insensitive to α . However, compared to the electron heating case, all of the distributions are much wider and peak at higher values, ~ 1.5 for $\beta = 0$ and > 2 for $\beta = 1$. Furthermore, in the $\beta = 1$ case, the $\alpha = -2.5$ distribution peaks at lower values compared $\alpha = -1.5, -2.0$.

Turning to the right hand panels, in the single-fluid model for $t_N \leq 4000$ s, the results cluster just near 1.0, though the $t_N = 3000$ s distribution is slightly bimodal, peaking strongly at ~ 0.75 and more weakly at ~ 1.25 . Additionally, the $t_N = 5000$ s case peaks slightly higher at ~ 1.5 and does not “pile up” near 1.0 as the other values of t_N do. For electron heating, the $t_N = 3000$ s distribution has a very strong and narrow peak at ≈ 0.5 while all of the other distributions peak at ~ 1 . For $t_N \geq 3000$ s, the location of the peak increases weakly with increasing t_N though this is not the case for $t_N = 1000, 2000$ s. Finally, for ion heating the distributions for each value of t_N are much wider than for a single fluid and electron heating and the peak values show a stronger dependence on t_N . The range of peak values is also much larger, with the $t_N = 1000$ s case peaking near 0 and the $t_N = 5000$ s case peaking at ~ 2 . As in [Figure 8](#), we see that the $t_N = 3000$ s distribution is bimodal. In general, the distributions grouped by t_N for all three heating types have a positive skew and are peaked in the range $\sim 0.5 - 1.5$ except for some extreme case in the ion heating scenario.

These results suggest that the emission measure ratio is generally in the range $\sim 0.5 - 1.5$, with some higher values. Given the uncertainties in the atomic physics in particular, this seems to support the conclusion of the presence of nanoflare heating by [Brosius et al. \(2014\)](#). Thus the calculation of such ratios from limited data has the potential to be a powerful diagnostic of the existence of nanoflare heating. Whether one can say more about the precise form of nanoflare heating is less clear. In these results the ratios are largely independent of the power-law index α and only weakly-dependent on the waiting time, t_N . Furthermore, the distributions are also weakly dependent on the relationship between the waiting time and heating rate, β . The exception is the ion heating case where the distributions are much wider, peak at higher values, and show a stronger dependence on α , β , and t_N . The problem with drawing conclusions from the details of these results lies in the numerous uncertainties in any data, especially concerning atomic physics.

4. CONCLUSIONS

In this paper we have carried out two-fluid modeling of nanoflare trains in AR cores and considered a range of models for the nanoflare energy distribution and timing as well as preferential heating of different species. For each set of parameters we have generated the emission measure distribution as a function of temperature. If the peak of the emission measure occurs at $T = T_m$, then we found that T_m and $EM(T_m)$ were independent of the properties of the nanoflare train and which species was heated. As a consequence, we demonstrated that the form of $EM(T)$ on either side of T_m reflected different aspects of the heating process. Below T_m the principle factor in determining $EM(T)$ is the presence of a waiting time between nanoflares: the high densities below T_m mean that species temperature equilibration has occurred so that no information about which species was heated remains.

Above T_m , higher temperatures arise when a power-law distribution of energy is assumed than for a nanoflare train with uniform heating rates. However, no information about the presence of a waiting time survives. Higher observed temperatures also arise for the single-fluid and electron heating cases where a “hot shoulder” can occur in $EM(T)$ at $T \sim 10$ MK. This is compared to the ion heating case where a finite equilibration time means that the electrons are heated more slowly. We find that, unlike some of the examples in [Paper I](#), NEI is not a major consideration, a constant

nanoflare train being the exception.

Two possible ways to relate these results to present and future observations were discussed. First we showed that while below T_m the well-known relation $EM \sim T^a$ was quite robust, that was not the case above T_m . On the other hand the calculation of a ratio between the emission measure at a pair of temperatures above and below T_m held more promise. For a wide range of parameters the ratio of the emission measure at two temperatures, $T_{hot} = 10^{6.9} > T_m$ and $T_{cool} = 10^{6.2} < T_m$, was of order unity, consistent with Brosius et al. (2014) within various errors. Further observational evidence of such ratios would, in our view, provide a very strong case for the presence of nanoflare heating. On the other hand, given the uncertainties in atomic physics and emission measure analysis, such a comparison seems unlikely to be able to shed more detailed light on the details (e.g. t_N , α , β) of the actual heating process.

It is clear from this and the preceding paper that characterization of this “hot” component is extremely challenging for a multiplicity of reasons. Progress is likely to come from the good spectral coverage of the MaGIXS instrument, and in particular from a space-based successor which could confirm beyond doubt the presence of the hot component and perhaps measure the predicted features of $EM(T)$. In the absence of complete spectral coverage, we propose a pair of metrics for the “hot” coronal component. Of particular interest is the ratio of pairs of emission lines characteristic of cool and hot plasma, as was recently discussed by Brosius et al. (2014). When high temperature spectral coverage is limited, information from high-energy instruments (Ishikawa et al. 2014; Hannah et al. 2016; Grefenstette et al. 2016) would be then desirable, but the energies of interest (≈ 1 keV) are highly challenging. In any event, complete wavelength coverage seems essential, something that we noted stellar astronomers have had for decades.

WTB was provided travel support to the Coronal Loops Workshop VII held in Cambridge, UK, at which a preliminary version of this work was presented, by NSF award number 1536094. This work was supported in part by the Big-Data Private-Cloud Research Cyberinfrastructure MRI-award funded by NSF under grant CNS-1338099 and by Rice University.

Software: astroML (VanderPlas et al. 2012), IPython (Pérez & Granger 2007), Jupyter notebook, matplotlib (Hunter 2007), NumPy, seaborn (Waskom et al. 2016), scipy (van der Walt et al. 2011)

REFERENCES

- Antiochos, S. K., & Sturrock, P. A. 1978, *The Astrophysical Journal*, 220, 1137
- Barnes, W. T., Cargill, P. J., & Bradshaw, S. J. 2016, *ArXiv e-prints*, 1608, arXiv:1608.04776
- Bradshaw, S. J. 2009, *Astronomy and Astrophysics*, 502, 409
- Bradshaw, S. J., & Cargill, P. J. 2006, *Astronomy and Astrophysics*, 458, 987
- . 2013, *The Astrophysical Journal*, 770, 12
- Bradshaw, S. J., Klimchuk, J. A., & Reep, J. W. 2012, *The Astrophysical Journal*, 758, 53
- Brosius, J. W., Daw, A. N., & Rabin, D. M. 2014, *The Astrophysical Journal*, 790, 112
- Cargill, P. 2013, *Nature*, 493, 485
- Cargill, P. J. 1994, *The Astrophysical Journal*, 422, 381
- . 2014, *The Astrophysical Journal*, 784, 49
- Cargill, P. J., Bradshaw, S. J., & Klimchuk, J. A. 2012a, *The Astrophysical Journal*, 752, 161
- . 2012b, *The Astrophysical Journal*, 758, 5
- Cargill, P. J., & Klimchuk, J. A. 2004, *The Astrophysical Journal*, 605, 911
- . 2006, *The Astrophysical Journal*, 643, 438
- Cargill, P. J., Warren, H. P., & Bradshaw, S. J. 2015, *Philosophical Transactions of the Royal Society of London Series A*, 373, 20140260
- Cirtain, J. W., Golub, L., Winebarger, A. R., et al. 2013, *Nature*, 493, 501
- Culhane, J. L., Harra, L. K., James, A. M., et al. 2007, *Solar Physics*, 243, 19
- Del Zanna, G., & Mason, H. E. 2014, *Astronomy and Astrophysics*, 565, A14
- Del Zanna, G., Tripathi, D., Mason, H., Subramanian, S., & O’Dwyer, B. 2015, *Astronomy and Astrophysics*, 573, A104
- Freedman, D., & Diaconis, P. 1981, *Zeitschrift für Wahrscheinlichkeitstheorie und Verwandte Gebiete*, 57, 453
- Grefenstette, B. W., Glesener, L., Krucker, S., et al. 2016, *The Astrophysical Journal*, 826, 20
- Guennou, C., Auchère, F., Klimchuk, J. A., Bocchialini, K., & Parenti, S. 2013, *The Astrophysical Journal*, 774, 31
- Hannah, I. G., Grefenstette, B. W., Smith, D. M., et al. 2016, *The Astrophysical Journal Letters*, 820, L14
- Hunter, J. D. 2007, *Computing in Science & Engineering*, 9, 90
- Ishikawa, S.-n., Glesener, L., Christe, S., et al. 2014, *Publications of the Astronomical Society of Japan*, 66, S15
- Jordan, C. 1975, *Solar Gamma-, X-, and EUV Radiation*, 68
- Klimchuk, J. A. 2006, *Solar Physics*, 234, 41
- Klimchuk, J. A., Patsourakos, S., & Cargill, P. J. 2008, *The Astrophysical Journal*, 682, 1351
- Kobayashi, K., Cirtain, J., Golub, L., et al. 2011, in *Society of Photo-Optical Instrumentation Engineers (SPIE) Conference Series*, Vol. 8147, 81471M
- Kosugi, T., Matsuzaki, K., Sakao, T., et al. 2007, *Solar Physics*, 243, 3
- Landi, E., Reale, F., & Testa, P. 2012, *Astronomy and Astrophysics*, 538, A111
- Miceli, M., Reale, F., Gburek, S., et al. 2012, *Astronomy and Astrophysics*, 544, A139
- Mulu-Moore, F. M., Winebarger, A. R., & Warren, H. P. 2011, *The Astrophysical Journal Letters*, 742, L6
- Parker, E. N. 1988, *The Astrophysical Journal*, 330, 474
- Pesnell, W. D., Thompson, B. J., & Chamberlin, P. C. 2012, *Solar Physics*, 275, 3

- Petralia, A., Reale, F., Testa, P., & Del Zanna, G. 2014, *Astronomy and Astrophysics*, 564, A3
- Pérez, F., & Granger, B. E. 2007, *Computing in Science & Engineering*, 9, 21
- Reale, F., & Orlando, S. 2008, *The Astrophysical Journal*, 684, 715
- Reale, F., Testa, P., Klimchuk, J. A., & Parenti, S. 2009, *The Astrophysical Journal*, 698, 756
- Reep, J. W., Bradshaw, S. J., & Klimchuk, J. A. 2013, *The Astrophysical Journal*, 764, 193
- Sanz-Forcada, J., Brickhouse, N. S., & Dupree, A. K. 2003, *The Astrophysical Journal Supplement Series*, 145, 147
- Scargle, J. D., Norris, J. P., Jackson, B., & Chiang, J. 2013, *The Astrophysical Journal*, 764, 167
- Schmelz, J. T., Asgari-Targhi, M., Christian, G. M., Dhaliwal, R. S., & Pathak, S. 2015, *The Astrophysical Journal*, 806, 232
- Schmelz, J. T., & Pathak, S. 2012, *The Astrophysical Journal*, 756, 126
- Schmelz, J. T., Saar, S. H., DeLuca, E. E., et al. 2009, *The Astrophysical Journal Letters*, 693, L131
- Testa, P., & Reale, F. 2012, *The Astrophysical Journal Letters*, 750, L10
- Testa, P., Reale, F., Landi, E., DeLuca, E. E., & Kashyap, V. 2011, *The Astrophysical Journal*, 728, 30
- Tripathi, D., Klimchuk, J. A., & Mason, H. E. 2011, *The Astrophysical Journal*, 740, 111
- Ugarte-Urra, I., & Warren, H. P. 2014, *The Astrophysical Journal*, 783, 12
- van der Walt, S., Colbert, S. C., & Varoquaux, G. 2011, *Computing in Science & Engineering*, 13, 22
- VanderPlas, J., Connolly, A., Ivezic, Z., & Gray, A. 2012, in *2012 Conference on Intelligent Data Understanding (CIDU)*, 47–54
- Viall, N. M., & Klimchuk, J. A. 2011, *The Astrophysical Journal*, 738, 24
- Warren, H. P., Brooks, D. H., & Winebarger, A. R. 2011, *The Astrophysical Journal*, 734, 90
- Warren, H. P., Winebarger, A. R., & Brooks, D. H. 2012, *The Astrophysical Journal*, 759, 141
- Waskom, M., Botvinnik, O., drewokane, et al. 2016, doi:10.5281/zenodo.45133
- Winebarger, A. R. 2014, *AGU Fall Meeting Abstracts*, 52, 03
- Winebarger, A. R., Schmelz, J. T., Warren, H. P., Saar, S. H., & Kashyap, V. L. 2011, *The Astrophysical Journal*, 740, 2
- Winebarger, A. R., Warren, H. P., Schmelz, J. T., et al. 2012, *The Astrophysical Journal Letters*, 746, L17